Unambiguous DFS Measurement System Based on an Integrated Photonic Chip With Wavelength-Selective Modulation

Mengya Zong, Jiaqi Shen, Shuang Wang, Yu Zhang, Xiangchuan Wang, Simin Li, and Shilong Pan, *Fellow, IEEE, Fellow, Optica*

***Abstract*—This paper presents and experimentally demonstrates a Doppler frequency shift (DFS) measurement system based on on-chip coherent wavelength-selective modulation, fabricated on a lithium niobate on insulator platform. The device employs a Mach-Zehnder interferometer-like structure with parallel arms, each consisting of a cascaded micro-ring resonator and phase modulator. By independently modulating the transmitted and echo signals on different wavelengths, the DFS is determined from the beat frequency generated between their corresponding sidebands. This methodology exhibits inherent robustness against both power fluctuations and wavelength-selection imperfections. Experimental characterization using 12 GHz, 15 GHz, and 18 GHz signals demonstrated a maximum measurement error within ±0.6 Hz over a DFS range of ±100 kHz. Simulation results further confirm the system's ability to distinguish between multiple moving targets with identical speeds but opposing directions.**

***Index Terms*—Doppler frequency shift measurement, integrated microwave photonics, lithium niobate on insulator, photonic chips.**

I. Introduction

OWING to the Doppler frequency shift (DFS) carrying important information of the radial velocity and direction for detecting moving targets, the measurement of DFS is widely applied in radars systems [1], [2], [3], autonomous vehicles [4], wireless communications [5], and electronic warfare applications [6]. However, with the increasing diversity of application scenarios and the growing complexity of electromagnetic environments, traditional electrical-based DFS measurement methods are limited by inherent electronic bottlenecks [7]. Over the past few decades, microwave photonic measurement techniques have emerged as a highly promising alternative, leveraging the intrinsic advantages of photonic systems, including large operational bandwidth, high-speed processing capabilities, low loss, and strong electromagnetic interference immunity [8], [9].

For microwave photonics-assisted DFS measurement methods, determining the absolute DFS value is relatively straightforward via heterodyne detection of the transmitted and reflected signals. However, the primary challenge lies in determining the directionality, which requires additional auxiliary approaches. Currently, three main techniques are employed: implementing in-phase/quadrature (I/Q) demodulation, utilizing reference signals, and employing optical frequency shift modules.

In the I/Q detection schemes, the determination of DFS direction depends on the phase timing relationship between the mixed signals from two parallel channels. The core of this method lies in introducing a stable and controllable 90° quadrature phase difference between the two signals. Various optical domain methods have been developed to generate this phase shift, such as introducing a 90° optical hybrid [10], utilizing the DC bias of the main modulator in a dual-parallel Mach-Zehnder modulator (DPMZM) [11], combining polarization quadrature processing with a Sagnac loop [12], and employing dispersion-compensating fibers [13]. This approach typically requires at least two photodetectors (PDs) to separately receive the orthogonal optical signals, along with a coherent waveform analyzer to demodulate the phase relationship between the two electrical channels, resulting in increased system complexity and cost.

The reference signal method introduces a known-frequency reference signal, which is mixed in the optical domain with the echo signal. By exploiting the beat frequency characteristics between the two signals, both the direction and magnitude of DFS can be determined [14], [15], [16], [17]. The system architecture requires only a single PD to accomplish the detection process, without the need for waveform analysis. However, it necessitates additional microwave oscillators or signal synthesizers to generate the reference signal. Furthermore, to achieve broadband detection, complex modulation schemes are typically employed, which increase the complexity of the device configuration.

The optical frequency-shifting technique typically modulates the transmitted and echo signals onto optical carriers with different wavelengths. It generates a low-frequency signal via optical heterodyning and compares its frequency to the preset frequency difference between the two optical carriers, thereby resolving the direction ambiguity of the DFS. Presently, this scheme employs a single laser as the light source. After beam

Received 29 October 2025; revised 16 January 2026; accepted 15 February 2026. Date of publication 24 February 2026; date of current version 16 May 2026. This work was supported in part by the National Key R&D Program of China under Grant 2022YFB2802704, and in part by the National Natural Science Foundation of China (NSFC) under Grant 62271249. *(Corresponding author: Simin Li.)*

The authors are with the National Key Laboratory of Microwave Photonics, Nanjing University of Aeronautics and Astronautics, Nanjing 210016, China (e-mail: myzong@nuaa.edu.cn; jqshen@nuaa.edu.cn; wangshuang37@nuaa.edu.cn; yu-zhang@nuaa.edu.cn; wangxch@nuaa.edu.cn; lisimin@nuaa.edu.cn; pans@nuaa.edu.cn).

Color versions of one or more figures in this article are available at https://doi.org/10.1109/JLT.2026.3667707.

Digital Object Identifier 10.1109/JLT.2026.3667707

splitting, an acousto-optic modulator (AOM) is used to introduce a predefined frequency shift, typically in the tens of MHz, onto one of the optical carriers [18], [19], [20], [21]. However, AOMs are susceptible to environmental disturbances, which can introduce measurement errors. Moreover, in multi-target detection scenarios, spectral overlap of the low-frequency signals may occur, leading to misinterpretation of the number of targets or their motion states.

At present, most DFS measurement schemes still rely on discrete components, which suffer from large footprint and limited stability. To promote system miniaturization, several on-chip solutions have been developed in recent years. For instance, [22] employs cascaded dual-drive Mach-Zehnder modulators (DDMZMs) together with a micro-ring resonator (MRR) for I/Q demodulation, while [23], [24] utilizes a reference signal with a DPMZM. In these on-chip architectures, high-performance optical modulators serve as the core devices of the DFS measurement system, decisively determining the signal processing bandwidth and precision. Leveraging its outstanding electro-optic performance, strong waveguide confinement, and CMOS compatibility, the lithium niobate on insulator (LNOI) platform provides an ideal physical foundation for achieving efficient linear modulation and dense integration. To date, LNOI-based photonic integrated devices have been comprehensively validated in fields such as microwave photonic signal generation [25] and high-performance radar systems [26].

This paper presents a novel on-chip architecture based on wavelength-selective modulation for DFS measurement. The chip features a Mach-Zehnder interferometer-like structure, with MRRs integrated at the input ports of phase modulators (PMs) on the upper and lower arms for wavelength selection. Proof-of-concept experiments conducted on the LNOI platform demonstrate that, at transmission frequencies of 12 GHz, 15 GHz, and 18 GHz, the system achieves high-precision measurement results with errors less than ±0.6 Hz within the DFS range of ±100 kHz. The proposed scheme demonstrates significant robustness in DFS detection, effectively suppressing the impact of power fluctuations and residual filtering interference and enables simultaneous detection of multiple moving targets, accurately distinguishing targets with identical velocities but opposite directional motions. Furthermore, by synergizing optical frequency comb technology with the tunability of MRRs, the architecture can extend operation to higher frequency bands while eliminating the requirement for high-frequency electrical local oscillators. This work establishes a reliable technical pathway toward advancing high-performance integrated DFS measurement systems.

II. Principle

The schematic diagram of the proposed integrated DFS measurement system is depicted in Fig. 1. It comprises three main modules: a source module, an on-chip modulation module, and a post-processing module. The on-chip modulation module, serving as the fundamental component, employs a Mach-Zehnder interferometer-like structure. Unlike conventional Mach-Zehnder modulators (MZMs), an add-drop MRR is integrated before the PM located in each of the upper and lower arms, enabling wavelength-selective modulation. Given

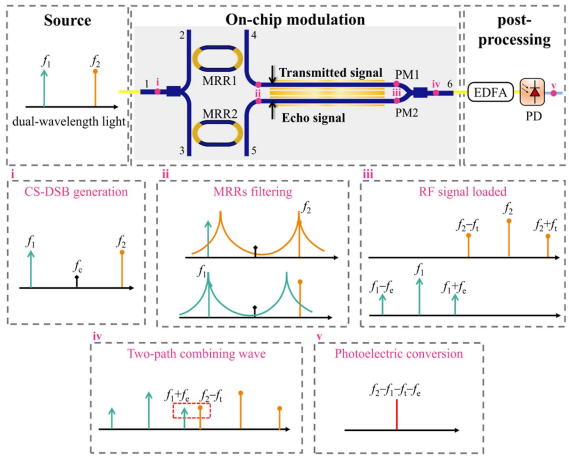

Fig. 1. Schematic and operation principles of the proposed DFS measurement system. MRR: micro-ring resonator; PM: phase modulator; EDFA: erbium-doped fiber amplifier; PD: photodetector.

that the transmission characteristics of the MRRs in the two arms are distinct, the source module must generate multi-wavelength coherent light, with two specific wavelengths aligned with the resonant peak of the corresponding MRR in each arm. The source module can be implemented using various methods, such as external modulation techniques, mode-locked fiber lasers, and optical frequency combs.

In this section, the external modulation technology is taken as an example to elaborate on the dual-wavelength coherent light generation. An external light with a central frequency of f_c is input into an MZM, which is biased to operate in the carrier-suppressed double-sideband (CS-DSB) mode. Under small signal modulation, the optical output of the MZM can be described by

$$E_{in}(t) = E_0 J_1(\gamma)\left[\exp(j2\pi f_1 t) + \exp(j2\pi f_2 t)\right], \quad (1)$$

where E_0 denotes the amplitude of external light, γ represents the modulation index of MZM. The frequencies f_1 and f_2 correspond to the $\pm 1^{st}$-order sidebands, explicitly defined as $f_1 = f_c - f_0$ and $f_2 = f_c + f_0$, where f_0 is the frequency of the radio frequency (RF) signal applied to the MZM. Note that f_c and f_0 are determined by the wavelength separation of the resonance peak between the two MRRs.

After coupling into the chip, the $\pm 1^{st}$-order optical sidebands are split into two paths by a 1×2 multimode interferometer (MMI). The MRRs filter the signals, selecting one sideband in each arm. The electric field can be expressed as

$$E_{upper}(t) \propto E_0 J_1(\gamma)\left[\alpha_{MRR1}\exp(j2\pi f_1 t) + \exp(j2\pi f_2 t)\right], \quad (2)$$

$$E_{\text{lower}}(t) \propto E_0 J_1(\gamma)\left[\exp(j2\pi f_1 t) + \alpha_{MRR2}\exp(j2\pi f_2 t)\right], \quad (3)$$

where the loss coefficients a_{MRR1} and a_{MRR2} indicate the amplitudes of unwanted sidebands after MRRs filtering, which are both approach zero in an ideal condition. The subsequent analysis of the modulation process in this section is based on this ideal condition.

In the upper path, the transmitted signal f_t is modulated onto the $+1^{st}$ optical sidebands by PM1; in the lower path, the echo signal f_e is modulated onto the -1^{st} optical sidebands by PM2. The mathematical expression can be written as

$$E_{upper}(t) \propto E_0 J_1(\gamma) \exp(j2\pi f_2 t) \cdot \exp[j\beta_1 \cos(2\pi f_t t)], \tag{4}$$

$$E_{lower}(t) \propto E_0 J_1(\gamma) \exp(j2\pi f_1 t) \exp[j\beta_2 \cos(2\pi f_e t + \varphi)], \tag{5}$$

where β_1 and β_2 are the modulation index of PM1 and PM2, respectively. φ is the relative phase difference between echo and transmitted signal.

Owing to the Doppler effect, a slight frequency shift arises between f_e and f_t, such that the DFS is expressed as

$$f_d = f_e - f_t, \tag{6}$$

where f_d takes a positive value when the moving target approaches the observer and a negative value when it recedes.

The two modulated optical signals are first combined using a 2×1 MMI and subsequently amplified by an erbium-doped fiber amplifier (EDFA). This composite signal is then fed into a PD, generating a low-frequency electrical signal that can be expressed as

$$i \propto \Re \cos[2\pi \Delta f t - (\varphi + \pi)], \tag{7}$$

where $\Re$ is the responsivity of the PD. The beat frequency Δf can be mathematically represented as

$$\begin{aligned} \Delta f &= f_2 - f_1 - f_t - f_e, \\ &= f_{\Delta\lambda} - 2f_t - f_d \end{aligned} \tag{8}$$

where $(f_2 - f_1)$ represents the frequency difference between the two wavelengths, denoted as $f_{\Delta\lambda}$. f_d can then be obtained from (8) as

$$f_d = f_{\Delta\lambda} - 2f_t - \Delta f, \tag{9}$$

Theoretically, given the known values of $f_{\Delta\lambda}$ and f_t, an unambiguous DFS detection can be achieved by comparing the magnitudes of Δf and $(f_{\Delta\lambda} - 2f_t)$. When Δf is less than $(f_{\Delta\lambda} - 2f_t)$, indicating a positive f_d, the moving target is approaching the observer; conversely, when Δf exceeds $(f_{\Delta\lambda} - 2f_t)$, indicating a negative f_d, the target is receding. Furthermore, as Δf is significantly lower than the transmitted signal f_t, the system achieves the mapping of DFS information to a low-frequency regime, thereby substantially alleviating the back-end signal processing pressure. More importantly, this frequency conversion effectively excludes transmitted and echo signal interference caused by leakage between the two modulated optical paths.

III. Experiment

A. Device Fabrication and Characterization

Fig. 2 presents the fabricated LNOI chip, occupying a compact footprint of 11.3 mm × 2.3 mm. The device was fabricated by IOPTEE using an x-cut wafer supplied by NANOLN. Fig. 2(b) provides a zoomed-in view of the MRRs. Each MRR has a racetrack circumference of 51.6 μm, a half-ring radius of 149.88 μm,

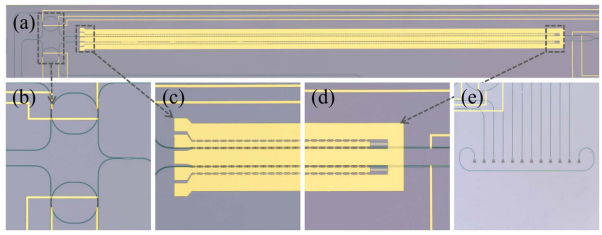

Fig. 2. Microscope image of the fabricated LNOI chip.

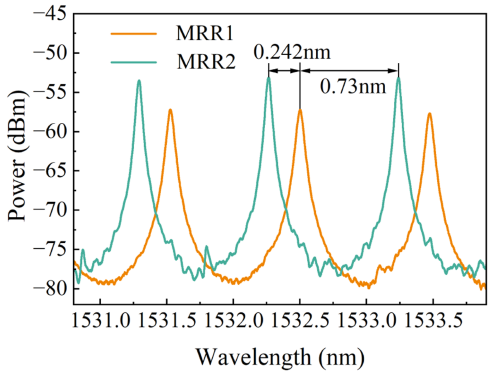

Fig. 3. Optical transmission responses of the MRRs.

and a 400 nm gap to the bus waveguide, resulting in a calculated optical path length of approximately 1045.45 μm. For active control, a thermal tuning electrode is integrated on each MRR, allowing for flexible adjustment of the resonance peak. Other key components, Fig. 2(c) and (d) present the GSGSG-type RF electrodes and 50-ohm impedance-matched electrodes designed on two parallel PMs, respectively. Fig. 2(e) shows the arrayed grating couplers (GCs), used for optical input/output, with their ports labeled 1–6 in Fig. 1.

Firstly, the optical transmission responses of the MRRs were characterized. To ensure long-term operational reliability and suppress MRRs wavelength drift caused by environmental temperature fluctuations, the chip was mounted on a thermoelectric cooler (TEC) during the experiment and its temperature was stabilized at 25 °C. The drop-port optical paths of MRR1 and MRR2 correspond to the routes from input port 2 to output port 4 and from input port 3 to output port 5, respectively, as shown in Fig. 1. In the experiment, an amplified spontaneous emission source (ASE-CL-100-SM-B) served as the optical input, and the drop port transmission spectra for the two MRRs were recorded using an optical spectrum analyzer (OSA, Yokogawa AQ6370D). The results are presented in Fig. 3. It can be observed that the free spectral range (FSR) for both MRRs was approximately 0.972 nm. The extinction ratio (ER) was measured to be ∼25 dB for MRR1 and ∼22 dB for MRR2, while their 3-dB bandwidths were approximately 7 GHz and 5 GHz, respectively. Furthermore, the wavelength separation between the resonance peaks of the two MRRs, denoted as $\Delta\lambda$, was characterized at two distinct values: 0.242 nm and 0.73 nm. These correspond to frequency separations $f_{\Delta\lambda}$ of approximately 31 GHz and 94 GHz, respectively. As observed in Fig. 3, a difference in insertion loss exists between MRR1 and MRR2. This is primarily attributable

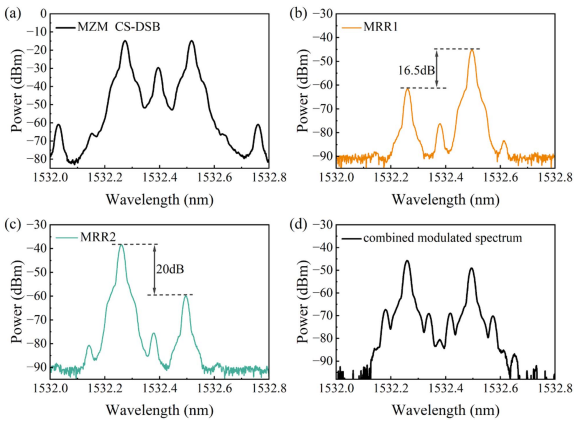

Fig. 4. (a) Spectrum of the generated dual-wavelength light source; drop-port output spectra of (b) MRR1 and (c) MRR2; (d) combined modulated spectrum of the two paths.

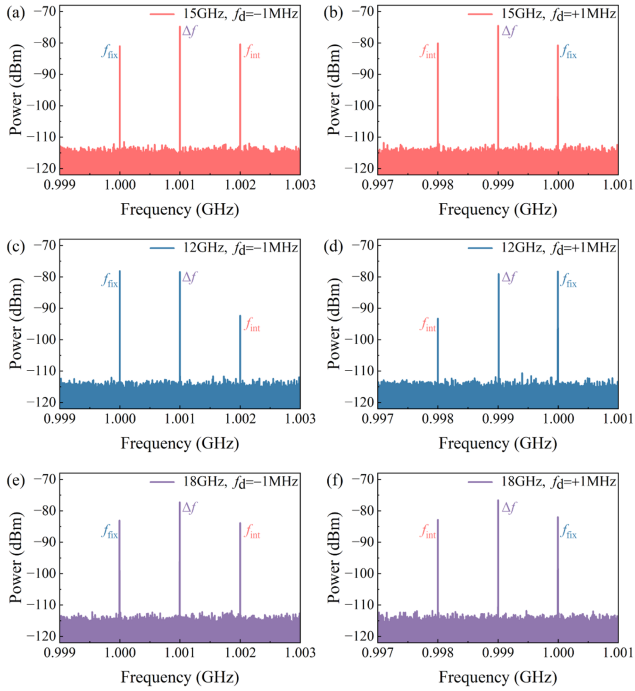

Fig. 5. Measured electrical spectra for: (a) 15 GHz, $f_d = -1$ MHz; (b) 15 GHz, $f_d = +1$ MHz; (c) 12 GHz, $f_d = -1$ MHz; (d) 12 GHz, $f_d = +1$ MHz; (e) 18 GHz, $f_d = -1$ MHz; (f) 18 GHz, $f_d = +1$ MHz.

to minor fluctuations in process parameters during fabrication, such as waveguide width, etching depth, and coupling gap, as well as factors like the alignment accuracy between the fiber array and the GCs during testing.

To validate the mode-selection performance of the MRRs, a dual-wavelength coherent light was generated using an external electro-optic modulator. A continuous-wave light at 14 dBm from a tunable laser source (Yenista TUNICS-T1005-HP) was injected into a MZM (Fujitsu FTM7938). Simultaneously, an RF signal (f_0) from a microwave source (Anapico APMS40G-4) was applied to the MZM, which was biased to operate in CS-DSB mode. To obtain a high-power new carrier, the ±1st-order sidebands were precisely aligned with the resonance peaks of the two MRRs. The optical carrier wavelength was set to 1532.383 nm and f_0 was set to 15.5 GHz (corresponding to half the frequency separation between the MRRs). The spectrum of the generated dual-wavelength coherent light is shown in Fig. 4(a). In practice, the MRRs function as optical filters within the system, and their 3-dB bandwidth allows for flexible adjustment of f_0 within a range of several GHz.

The off-chip light was then passed through a polarization controller and vertically coupled into the GCs on the chip via a fiber array. Fig. 4(b) and (c) illustrate the spectra of the dual-wavelength coherent light exiting through the drop ports of MRR1 and MRR2. The wavelength selection functionality of the MRRs is clearly observed: the suppression ratios for the non-selected wavelengths were measured to be 16.5 dB and 20 dB, which are lower than the ERs of the individual MRRs. This performance degradation is attributed to the partial spectral overlap between the two resonance peaks, leading to incomplete suppression of non-selected wavelengths. From a theoretical standpoint, this overlap means that the loss coefficients for the non-selected wavelengths, α_{MRR1} and α_{MRR2} (see (2) and (3)), do not approach zero.

B. DFS Detection

In the proof-of-concept experiment, two microwave signal generators (Rohde&Schwarz SMA100B) were employed to generate both the transmitted signal (f_t) and the simulated echo signal (f_e), each with an output power of 15 dBm. These two signals were then independently modulated onto two on-chip sub-PMs via an RF probe (MPI T26D-GSGSG0100). The off-chip light was coupled into the chip through input port 1, and after being combined by a 2 × 1 MMI, the modulated optical signal was coupled out from output port 6. The modulation spectrum is shown in Fig. 4(d). It was first amplified by an EDFA (Amonics AEDFA-PA-35-B-FA) for power compensation, followed by optoelectronic conversion via a PD (CETC GD45220R). Finally, the resulting electrical signal, containing DFS features, was measured using an electrical spectrum analyzer (ESA, Keysight N9020B). f_t was set to 15 GHz, and f_e was set to 14.999 GHz and 15.001 GHz, respectively, in order to simulate a DFS of ±1 MHz. According to (8), when f_d is −1 MHz, Δf is 1.001 GHz; when f_d is +1 MHz, Δf is 0.999 GHz. The corresponding spectral results are shown in Fig. 5(a) and (b).

In addition to the desired beat frequency Δf, two clutter signals, denoted as f_{fix} and f_{int}, were also observed in the output spectra. These signals arise due to the limited suppression ratio of the MRRs at non-selected wavelengths (corresponding to Fig. 4(b) and (c)). This incomplete suppression causes a portion of f_t to modulate the undesired -1^{st} order optical carrier, and similarly, a portion of f_e to modulate the $+1^{st}$ order carrier. As a result, these clutter components are generated according to $f_{\mathrm{fix}} = f_{\Delta\lambda} - 2f_t$ and $f_{\mathrm{int}} = f_{\Delta\lambda} - 2f_e$. However, these clutter signals do not impair unambiguous DFS detection. Since f_{fix} is a known and constant value (1 GHz in this case), the direction of the target motion can be determined by comparing the position of Δf relative to f_{fix}. For a negative DFS ($f_t > f_e$), the frequency

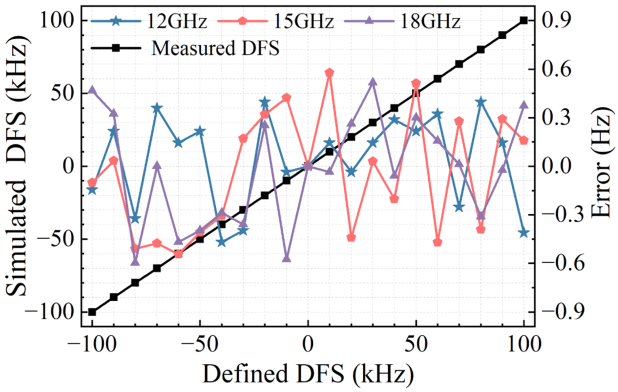

Fig. 6. Measured DFS and DFS error.

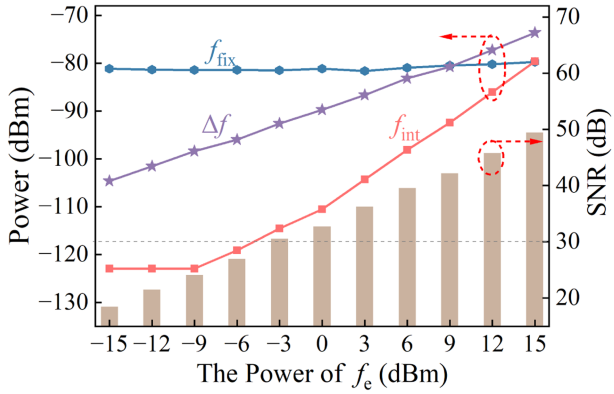

Fig. 7. Receiver sensitivity test results.

relationship is $f_{int} > \Delta f > f_{fix}$; conversely, for a positive DFS ($f_t < f_e$), it becomes $f_{int} < \Delta f < f_{fix}$.

To further extend the operational bandwidth, the frequency spacing $f_{\Delta\lambda}$ of the dual-wavelength coherent light was tuned by leveraging the 3-dB bandwidth of the MRRs. Specifically, by configuring $f_{\Delta\lambda}$ at 25 GHz and 37 GHz to match transmit signals of 12 GHz and 18 GHz, respectively, the system achieved unambiguous detection of DFS within a range of ±1 MHz, as illustrated in Fig. 5(c)–(f).

As illustrated in Fig. 5, the power levels of the three signals exhibit varying intensities across the transmitted frequencies. Specifically, Δf reaches its maximum power at the 15 GHz transmitted signal, which is primarily attributed to the optimized resonance matching and superior filtering efficiency of the MRRs at this frequency. The observed non-uniformity in the power consistency of f_{fix} and f_{int} stems from the disparate filtering slopes of the two MRRs, power imbalances between the dual-wavelength light and contact losses from the RF probe. Because the detection principle relies on the frequency ordering of the three signals rather than their power amplitudes, unambiguous DFS detection does not require high suppression ratios for the clutter components. The direction of the target can be correctly identified as long as the signal peaks are discernible, regardless of their relative power.

To quantify the DFS discrimination error, the system's performance was evaluated using transmitted signals at 12 GHz, 15 GHz, and 18 GHz. The simulated DFS was swept over a range of ±100 kHz in 10 kHz increments. Using an ESA with both resolution and video bandwidths set to 1 Hz to ensure high precision, the measured discrimination errors were within ±0.47 Hz, ±0.58 Hz, and ±0.6 Hz for the three respective carriers, as illustrated in Fig. 6. These minimal error margins confirm the high accuracy of the proposed architecture and demonstrate excellent consistency with theoretical expectations.

To evaluate the system's receiving sensitivity, the power of the simulated echo signal (f_e) was varied from –15 dBm to 15 dBm, while the transmitted signal (f_t) was maintained at 15 GHz with a constant power of 15 dBm. Fig. 7 plots the measured power of the resulting frequency components and the signal-to-noise ratio (SNR) of Δf. It can be observed that the power of f_{fix} remained consistently stable across the entire input power range, since its generation is independent of the power of f_e. This stability in both frequency and power renders f_{fix} an ideal benchmark, providing a constant reference value for comparison with Δf. By analyzing the difference between f_{fix} and Δf, the sign of the DFS can be unambiguously determined. In contrast, the power levels of both Δf and f_{int} rose proportionally with the power of f_e. Notably, when the power of f_e was less than 3 dBm, the power of Δf is substantially higher than that of f_{int}. This large power margin is highly advantageous, as it ensures reliable and high-fidelity DFS detection even for weak echo signals. As f_e power increases, the power gap between Δf and f_{int} narrows. Concurrently, the SNR of Δf steadily improves, surpassing 30 dB once the echo power exceeds −3 dBm.

This experiment confirms that the detection principle is fundamentally robust, as it relies on the fixed frequency relationship among the three spectral components (Δf, f_{int} and f_{fix}), not their absolute power. Consequently, the DFS information can be unambiguously determined from the relative positions of any two of these signals, underscoring the system's resilience to power fluctuations.

V. Discussion

A. MRR Performance Optimization

The performance of MRRs is critical to the overall system capability, as it directly influences the spectral purity of the measured signal, the flexibility of the operating frequency range, and the system stability.

Spectral purity is contingent upon the filtering characteristics of the MRR, which are in turn closely related to the MRR's quality factor (Q-value) and ER. As evidenced by prior experiments, the finite suppression ratio of MRRs induces the generation of clutter signals (f_{fix} and f_{int}). Although these artifacts do not compromise single-target DFS detection, their presence complicates the output spectrum and could lead to detection ambiguity in more complex scenarios, such as multi-target detection. Therefore, mitigating these clutter signals is essential for advancing the system's capabilities.

Fundamentally, this issue can be addressed by co-optimizing the MRR's Q-value and ER: increasing the Q-value enhances the selectivity for the target wavelengths and reduces spectral

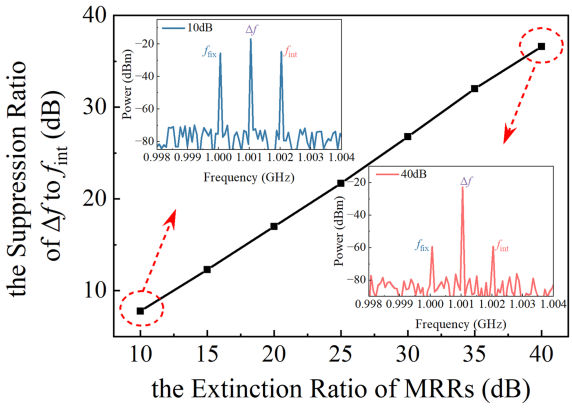

Fig. 8. The suppression ratio of Δf to f_{int} versus the extinction ratio of MRRs.

overlap and improving the ER suppresses the response at non-selected wavelengths, thereby yielding a purer signal component in the beat-frequency spectrum. This section focuses on analyzing the suppression of target signals relative to clutter signals as the extinction ratio increases.

The simulation parameters were configured to strictly align with the experimental conditions: the transmitted and echo signal frequencies were set to 15 GHz and 14.999 GHz, respectively. The ER was varied from 10 dB to 40 dB in 5 dB increments. Notably, this simulation adopts idealized assumptions, disregarding potential asymmetries in power and extinction ratios between the two MRRs. Thus, the powers of f_{fix} and f_{int} are considered equal, and f_{int} is used as the reference for evaluating clutter suppression. As illustrated in Fig. 8, increasing the MRR ER effectively suppresses interference from the f_{int} and f_{fix} clutter components. In practice, a higher ER can be achieved by optimizing the MRR coupling region design or by cascading multiple MRRs.

The working bandwidth of the system can be expanded and optimized through the tunability of the MRR resonance peak. This is achieved by integrating thermal tuning electrodes onto the MRRs, which allows for precise adjustment of the frequency separation ($f_{\Delta\lambda}$). This capability enables the system to accommodate a wide range of transmitted signal frequencies, thereby supporting future scalability to broader bandwidth applications.

When the thermal tuning function of MRRs is engaged in system measurements, the potential issues of thermal crosstalk and wavelength drift merit significant attention. Significant wavelength drift or thermal crosstalk in the system would introduce uncertainty in both the wavelength spacing of the multi-wavelength light source and the frequency configurations of the transmitted signal, thereby restricting functional versatility and undermining long-term operational stability. Consequently, ensuring reliable performance requires the simultaneous mitigation of wavelength instability and the suppression of thermal coupling. Future research efforts will proceed along the following two parallel directions: on the one hand, maintaining resonant wavelength stability through real-time wavelength locking or TEC-based temperature control strategies; on the other hand, optimizing the chip layout design by increasing ring separation or incorporating thermal isolation structures to minimize crosstalk effects.

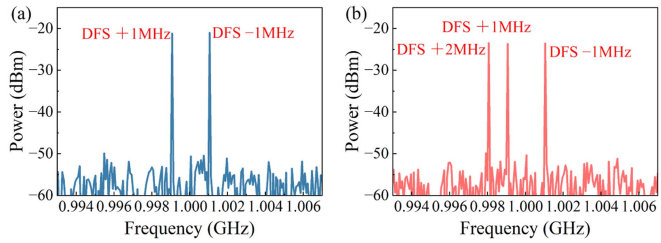

Fig. 9. Multi-moving targets detection results.

B. Multi-Targets DFS Detection

With an adequately optimized MRR suppression ratio, the proposed scheme can achieve simultaneous detection of multiple moving targets. A key advantage of this system is its capability to unambiguously distinguish between targets moving at the identical speed but in opposite directions. This section verifies this multi-target detection capability through a series of simulations. In the simulations, multiple echo signals were injected into the PM via an N×1 coupler. The results for dual-target and triple-target detection scenarios are presented in Fig. 9. For the dual-target case, as shown in Fig. 9(a), two echo signals at 14.999 GHz and 15.001 GHz were used, corresponding to the DFS of ±1 MHz. For the triple-target case shown in Fig. 9(b), three echo signals at 14.998 GHz, 14.999 GHz, and 15.001 GHz were simulated, corresponding to DFS of −2 MHz, −1 MHz, and +1 MHz, respectively.

C. Compare With Previous Works

In order to provide a visual illustration of the features of the DFS measurement scheme presented in this paper, Table I compares our work with previous approaches in terms of system architecture, technology, working bandwidth, measurement error.

As summarized in Table I, compared to existing schemes, this work proposes a novel on-chip integrated architecture that represents a departure from the simple migration of discrete systems. Based on a parallel "MRR-PM" configuration, the architecture enables wavelength-selective as well as independent modulation of transmitted and echo signals. By synergizing optical frequency comb technology with the tunability of MRRs, this wavelength-selective modulation architecture achieves a wide operational frequency range without requiring high-frequency electrical local oscillators. Furthermore, the streamlined architecture exhibits strong robustness against signal power fluctuations and system performance interference. It facilitates the mapping of DFS information to a low-frequency regime, thereby alleviating the back-end signal processing load and supporting simultaneous multi-target detection. This approach not only effectively addresses the inherent constraints of discrete systems, including excessive bulk, high cost, substantial power consumption, and instability, but also demonstrates compatibility across various material platforms.

V. Conclusion

In conclusion, this work introduces and experimentally validates an unambiguous DFS detection method based on coherent

TABLE I
COMPARISON OF PREVIOUS WORKS AND THIS WORK

Ref.	Size	Architecture	Technology	Working bandwidth /GHz	Measurement error/Hz
[10]	Discrete device	PloM+MZM+Optical hybrid	I/Q	10–38	±5.8
[13]	Discrete device	PM*2+ dispersion medium	I/Q	10–14	—
[14]	Discrete device	DPMZM+DDMZM+3*90° hybrid	Reference signal	7–16	±0.05
[16]	Discrete device	DPMZM	Reference signal	15	±0.8
[20]	Discrete device	PM1+AOM+PM2	Optical frequency shift	10–12	±0.7
[22]	Partial integration (SOI)	DDMZM*2+MRR	I/Q	10–20	±0.028
[23]	Partial integration (LNOI)	DPMZM	Optical frequency shift	5–30	±0.3
[24]	Partial integration (LNOI)	DPMZM+DPMZM	Reference signal	16	—
This work	Partial integration (LNOI)	MRR*2+PM*2	Wavelength selective modulation	12–18	±0.6

Note: PloM: polarisation modulator

wavelength-selective modulation. Fabricated on a LNOI platform, the proposed integrated chip incorporates a Mach-Zehnder interferometer-like structure with cascaded MRRs and PMs in a parallel configuration. An advantage of this architecture is its enhanced robustness. The detection scheme determines the DFS by relying on invariant relationships among frequency components rather than absolute power levels, thereby exhibiting strong immunity to both signal power fluctuations and residual interference from imperfect wavelength selection. System validation was conducted using transmitted signals at 12 GHz, 15 GHz, and 18 GHz, achieving measurement errors within ±0.6 Hz over a ±100 kHz range. Simulation results indicate that enhancing the performance of the MRRs enables precise discrimination of DFS for multiple targets, including those moving at identical speeds but in opposite directions. Furthermore, combining optical frequency combs with the tunability of MRRs provides the system with extensive frequency scalability. With most functional elements integrated monolithically, the system offers substantial benefits in compactness, cost efficiency, and power consumption, providing a practical and scalable solution for highly integrated DFS measurement applications demanding high performance.

REFERENCES

[1] V. C. Chen, F. Li, S.-S. Ho, and H. Wechsler, "Micro-doppler effect in radar: Phenomenon, model, and simulation study," *IEEE Trans. Aerosp. Electron. Syst.*, vol. 42, no. 1, pp. 2–21, Jan. 2006.

[2] S. M. Li et al., "Chip-based microwave-photonic radar for high-resolution imaging," *Laser Photon. Rev.*, vol. 14, no. 10, Oct. 2020, Art. no. 1900239.

[3] F. Z. Zhang et al., "Photonics-based broadband radar for high-resolution and real-time inverse synthetic aperture imaging," *Opt Exp.*, vol. 25, no. 14, pp. 16274–16281, Jul. 2017.

[4] Z. Tang and S. Pan, "Simultaneous measurement of doppler-frequency-shift and angle-of-arrival of microwave signals for automotive radars," in *Proc. Int. Top. Meeting Microw. Photon.*, Oct. 2019, pp. 1–4.

[5] L. H. Wang, X. C. Wang, and S. L. Pan, "Microwave photonics empowered integrated sensing and communication for 6G," *IEEE Trans. Microw. Theory Tech.*, vol. 73, no. 8, pp. 5295–5315, Aug. 2025.

[6] A. E. Spezio, "Electronic warfare systems," *IEEE Trans. Microw. Theory Techn.*, vol. 50, no. 3, pp. 633–644, Mar. 2002.

[7] J. P. Yao and J. Capmany, "Microwave photonics," *Sci. China Inf. Sci.*, vol. 65, no. 12, Dec. 2022, Art. no. 221401.

[8] S. Pan and J. Yao, "Photonics-based broadband microwave measurement," *J. Lightw. Technol.*, vol. 35, no. 16, pp. 3498–3513, Aug. 2017.

[9] X. Zou, B. Lu, W. Pan, L. Yan, A. Stöhr, and J. Yao, "Photonics for microwave measurements," *Laser Photon. Rev.*, vol. 10, no. 5, pp. 711–734, Sep. 2016.

[10] B. Lu et al., "Wideband microwave Doppler frequency shift measurement and direction discrimination using photonic I/Q detection," *J. Lightw. Technol.*, vol. 34, no. 20, pp. 4639–4645, Oct. 2016.

[11] W. Chen et al., "Wideband Doppler frequency shift measurement and direction discrimination based on a DPMZM," *IEEE Photon. J.*, vol. 9, no. 2, Apr. 2017, Art. no. 5501008.

[12] K. Zhang et al., "Photonic approach to wideband Doppler frequency shift estimation system based on a DPMZM and a Sagnac loop," *Optik - Int. J. Light Electron Opt.*, vol. 182, pp. 219–226, Jan. 2019.

[13] C. Y. Yi, H. Chi, and T. Jin, "A photonic approach for Doppler frequency shift measurement with dispersion medium," *IEEE Photon. J.*, vol. 12, no. 5, Oct. 2020, Art. no. 7102708.

[14] P. Zuo and Y. Chen, "Photonic-assisted filter-free microwave Doppler frequency shift measurement using a fixed low-frequency reference signal," *J. Lightw. Technol*, vol. 38, no. 16, pp. 4333–4340, Aug. 2020.

[15] G. Y. Li, D. F. Shi, L. Wang, M. Li, N. H. Zhu, and W. Li, "Photonic system for simultaneous and unambiguous measurement of angle-of-arrival and Doppler-frequency-shift," *J. Lightw. Technol.*, vol. 40, no. 8, pp. 2321–2328, Apr. 2022.

[16] Y. C. Yang, C. Du, D. Wang, M. H. Wang, and W. Dong, "Simple Doppler frequency shift measurement scheme based on microwave photonics," *IEEE Photon. Technol. Lett.*, vol. 34, no. 1, pp. 67–70, Jan. 2022.

[17] Q. Q. Jia, J. Y. Li, L. C. Sun, D. C. Li, and J. G. Liu, "A simple photonics-based measurement method for microwave DFS and AOA," *IEEE Photon. J.*, vol. 14, no. 3, Jun. 2022, Art. no. 5532108.

[18] B. Lu, W. Pan, X. H. Zou, X. L. Yan, L. S. Yan, and B. Luo, "Wideband Doppler frequency shift measurement and direction ambiguity resolution using optical frequency shift and optical heterodyning," *Opt. Lett.*, vol. 40, no. 10, pp. 2321–2324, May 2015.

[19] C. Y. Yi, H. Chi, B. Yang, and T. Jin, "A PM-based approach for Doppler frequency shift measurement and direction discrimination," *Opt. Commun.*, vol. 458, Mar. 2020, Art. no. 124796.

[20] J. M. Qian, L. Li, Y. X. Jiang, C. B. Lei, and X L., "Photonic scheme for the simultaneous measurement of Doppler frequency shift and angle of arrival based on optical frequency shift heterodyne and power mapping," *Opt. Exp.*, vol. 32, no. 22, pp. 39950–39962, Oct. 2024.

[21] Y. S. Gao et al., "Wideband anti-interference microwave photonic measurement for Doppler frequency shift and angle of arrival," *IEEE Trans. Instrum. Meas.*, vol. 73, 2024, Art. no. 8001508.

[22] L. Tang, Z. Tang, S. Li, S. Liu, and S. Pan, "Simultaneous measurement of microwave Doppler frequency shift and angle of arrival based on a silicon integrated chip," *IEEE Trans. Microw. Theory Tech.*, vol. 70, no. 9, pp. 4243–4250, Sep. 2022.

[23] J. M. Tao et al., "Thin-film lithium niobate dual-parallel Mach-Zehnder modulator for a simple photonic system measuring Doppler frequency shift," *Chin. Opt. Lett.*, vol. 22, no. 9, Sep. 2024, Art. no. 090005.

[24] W. J. Zhao, X. X. Yao, C. Yu, S. M. Li, and S. L. Pan, "A photonic-assisted transceiver for microwave Doppler frequency shift measurement," in *Proc. SPIE*, vol. 11902, no. 119020W, Oct. 2021, Art. no. 119020W.
[25] R. Ma et al., "Ka-band thin film lithium niobate photonic integrated optoelectronic oscillator," *Photon. Res*, vol. 12, no. 6, pp. 1283–1292, Jun. 2024.
[26] S. Zhu et al., "Integrated lithium niobate photonic millimetre-wave radar," *Nature Photon.*, vol. 19, no. 2, pp. 204–211, Jan. 2025.

Mengya Zong received the B.E. degree from Huaibei Normal University, Huaibei, China, in 2020 and the M.E. degree in 2023, from the Beijing University of Technology, Beijing, China, where she is currently working toward the Ph.D. degree with the Nanjing University of Aeronautics and Astronautics, Nanjing, China. Her research focuses on integrated microwave photonics.

Jiaqi Shen received the B.S. degree from Tiangong University, Tianjin, China, in 2022 and the M.E. degree in 2025, from the Nanjing University of Aeronautics and Astronautics, Nanjing, China, where he is currently working toward the Ph.D. degree in electronic science and. His research focuses on integrated microwave photonics.

Shuang Wang received the B.S. degree in electronic information science and technology and the M.S. degree in electronic science and technology from the Nanjing University of Aeronautics and Astronautics, Nanjing, China, in 2022 and 2025, respectively. Her research focuses on integrated microwave photonics.

Yu Zhang received the B.S. degree in electronic science and technology in 2025, from the Nanjing University of Aeronautics and Astronautics, Nanjing, China, where she is currently working toward the Ph.D. degree. Her research focuses on integrated microwave photonics.

Xiangchuan Wang received the B.E. degree in automation and the Ph.D. degree in microelectronics and solid-state electronics from Nanjing University, Nanjing, China, in 2009 and 2015, respectively. He is currently a Professor with the National Key Laboratory of Microwave Photonics, Nanjing University of Aeronautics and Astronautics, Nanjing. He has authored and coauthored more than 80 research papers. His research interests include microwave photonics measurement and radar.

Simin Li received the B.S. and Ph.D. degrees from Nanjing University, Nanjing, China, in 2009 and 2014, respectively. She is currently an Associate Professor with the National Key Laboratory of Microwave Photonics, Nanjing University of Aeronautics and Astronautics, Nanjing. Her research interests include integrated microwave photonic devices and systems.

Shilong Pan (Fellow, IEEE) is currently a Professor with the Nanjing University of Aeronautics and Astronautics, Nanjing, China. His research focuses on microwave photonics, which includes optical generation and processing of microwave signals, analog photonic links, photonic microwave measurement, and integrated microwave photonics. He has authored or coauthored more than 350 papers in peer-reviewed journals.

He is currently the Senior Editor of *PhotoniX*, an Associate Editor for IEEE/OPTICA JOURNAL OF LIGHTWAVE TECHNOLOGY and IEEE TRANSACTIONS ON MICROWAVE THEORY AND TECHNIQUES, and Vice Chair of IEEE MTT-22 Microwave Photonics. He was also the Chair of a number of international conferences, symposia, and workshops, including the TPC Chair of IEEE ICOCN 2015, TPC chair of IEEE MWP 2023, TPC Co-chair of IEEE MWP 2017, and General Co-chair of IEEE MWP 2021 and 2025.

Prof. Pan is a Fellow Optica and SPIE. He was selected as an IEEE Photonics Society Distinguished Lecturer in 2019 and an IEEE MTT-S Distinguished Microwave Lecturer in 2022, and was the recipient of IEEE MTT-S Outstanding Young Engineer Award in 2021.